

Cell-projection pumping: A hydrodynamic cell-stiffness dependent mechanism for cytoplasmic transfer between mammalian cells

Hans Zoellner^{1,2*}, Navid Paknejad³, James Cornwell¹, Belal Chami¹, Yevgeniy Romin³, Vitaly Boykov³, Sho Fujisawa³, Elizabeth Kelly¹, Garry W. Lynch⁴, Glynn Rogers¹, Katia Manova³, Malcolm A.S. Moore²

¹ The Cellular and Molecular Pathology Research Unit, Oral Pathology and Oral Medicine, School of Dentistry, Faculty of Medicine and Health, The University of Sydney, Westmead Hospital, Westmead, NSW 2145, Australia

² Cell Biology, The Memorial Sloan Kettering Cancer Center, 430 E 67th St, RRL 717, New York, NY

³ Molecular Cytology, The Memorial Sloan Kettering Cancer Center, 415-417 E 68 Street, ZRC 1962, New York, NY

⁴ Sydney Medical School, Faculty of Medicine and Health, and Sydney School of Veterinary Science, Faculty of Science, The University of Sydney, NSW, 2006, Australia

Corresponding Author: H Zoellner

The Cellular and Molecular Pathology Research Unit, Oral Pathology and Oral Medicine, School of Dentistry, Faculty of Medicine and Health Sciences, The University of Sydney, Westmead Hospital, Westmead, NSW 2145, Australia

Email: hans.zoellner@sydney.edu.au

Ph: +61 2 8890 7892,

FAX: +61 2 9893 8671

Abstract

We earlier reported cytoplasmic fluorescence exchange between cultured human fibroblasts and malignant cells (MC). Current time-lapse microscopy showed most exchange was from fibroblasts into MC, with less in the reverse direction. We were surprised transfer was not via tunneling nanotubes as described by others, but was instead via fine and often branching cell projections that defied direct visual resolution because of their size and rapid movement. Their structure was revealed nonetheless, by their organellar cargo and the grooves they formed indenting MC, while transfer events coincided with rapid retraction of the cell-projections. This suggested a hydrodynamic mechanism that could be tested by mathematical modelling. Increased hydrodynamic pressure in retracting cell-projections, normally returns cytoplasm to the cell body. We hypothesize 'cell-projection pumping' (CPP), where cytoplasm in retracting cell-projections partially equilibrates into adjacent recipient cells via temporary inter-cellular cytoplasmic continuities. Plausibility for CPP was explored via a mathematical model, which predicted preferential CPP into cells with lower cell stiffness, since pressure equilibrates towards least resistance. Predictions from the model were satisfied when fibroblasts were co-cultured with MC, and fluorescence exchange related with cell stiffness measured by atomic force microscopy. When transfer into 5000 simulated recipient MC or fibroblasts was studied in computer simulations, inputting experimental cell stiffness and donor cell fluorescence values generated transfers to simulated recipient cells similar to those seen by experiment, including an expected inverse relationship between receptor cell stiffness and fluorescence uptake. We propose CPP as a novel mechanism in mammalian inter-cellular cytoplasmic transfer and communication.

1 Introduction

We earlier described the exchange of fluorescently labeled membrane and cytoplasmic protein, as well as alkaline phosphatase between cultured human fibroblasts and malignant cells (MC) ¹, and others have made similar observations ²⁻¹³. Notably, we found altered phenotype subsequent to

inter-cellular transfer, and recognize implications for cancer biology, inflammation, wound healing and development^{1,14,15}.

Cytoplasmic transfer modulating phenotype is described as being via plasmodesmata in plants, septal pores in fungi, and tunneling nanotubes (TNT) in mammalian cells^{12,16,17}. Further, there are numerous reports of mitochondrial exchange between mammalian cells by a still uncertain mechanism, and this too can affect cell phenotype^{5-10,18}.

TNT are long straight tube-like connections that establish cytoplasmic continuity between individual cells, and are known to mediate exchange of cytoplasm and organelles. When seen in cell culture, TNT are typically suspended above the culture substrate, and have the appearance of taught wire-like connections. They appear to be drawn out from pre-existing inter-cellular cytoplasmic continuities, when adjacent and touching cells separate and migrate from one another, but may also form by association of adjacent filopodia^{11-13,16,19-23}. Interestingly, TNT-mediated organelle transfer occurs via active ATP dependent mechanisms¹¹⁻¹³. Although other cell-projections are not considered capable of similar transfer²⁴, short-straight TNT-like structures mediating exchange have been described by some authors as ‘microtubules’², which should not to be confused with the separate cytoskeletal structures also termed ‘microtubules’. In addition to inter-cellular cytoplasmic exchange via TNT, exosomes and other shed micro-vesicular structures can mediate the transfer of material from one cell to another, and this can affect cell phenotype^{19,25}, but as will be seen below, neither TNT or exosomes contributed significantly to inter-cellular cytoplasmic exchange in our experiments.

Here we describe confocal laser scanning microscopy (CLSM) studies, initiated to address the possibility that TNT were responsible for the inter-cellular exchange process we previously observed¹. As will be apparent from results shown below, time-lapse microscopy excluded a role for TNT and revealed that exchange occurred during apparently spasmodic retraction of donor cell-projections instead.

The transferring cell-projections could not be resolved to a high degree of accuracy, because of their rapid movement, paucity of fluorescent labelling, and limitations of CLSM. Images did, however, suggest a hypothesis for hydrodynamic transfer of cytoplasm from donor cell-projections into receptor cells, for which we propose the term ‘cell-projection pumping’ (CPP).

Limitations of microscopy led us to apply a modelling strategy to explore plausibility of CPP. In brief, we: a) developed a mathematical model for CPP; b) determined if predictions from that model relating cell stiffness with fluorescence transfer were satisfied by experiment; and c) used experimental cell stiffness and fluorescence data to construct computer simulated populations of cells exchanging cytoplasm by CPP, to determine if simulation results similar to experimental observations could be achieved making biologically reasonable assumptions for variables in the mathematical model.

With regard to the fluorescent microscopy work described below, it is important to appreciate necessity to use permanent labels, such as the fluorescent lipophilic markers DiD and DiO to demonstrate total cytoplasmic transfer, because such labels persist long after degradation of the originally labelled structures. By contrast, cell turn-over renders highly specific organellar or protein labels unreliable for detecting cumulative cytoplasmic transfer between cells. Also important is that fibroblasts have appreciably greater cell surface stiffness compared with MC²⁶.

2 Materials and Methods

2.1 Materials

All culture media including M199, DMEM- α Trypsin (0.25%)-EDTA (0.02%) and phosphate buffered saline (PBS), as well as Penicillin (10,000 U/ml)-Streptomycin (10,000 μ g/ml) concentrate solution were prepared and supplied by the Memorial Sloan-Kettering Cancer Centre Culture Media Core Facility (New York, NY). Amphotericin B was purchased from Life Technologies (Grand Island, NY). Gelatin was from TJ Baker Inc (Philipsburgh, NJ). Bovine serum albumin was from Gemini Bioproducts (West Sacramento, CA). Falcon tissue culture flasks, Atomic Force Microscopy (AFM) dishes and centrifuge tubes were purchased from BDBiosciences (Two Oak Park, Bedford, MA). Culture well coverslips were from Lab-Tek (Rochester, NY). Human dermal fibroblasts were from The Coriell Institute (Camden, NJ). SAOS-2 osteosarcoma cells were from

the American Type Culture Collection (VA, USA). MM200-B12 melanoma cells from The Millennium Institute (Westmead, NSW, Australia). The fluorescent labels 1,1'-dioctadecyl-3,3,3',3'-tetramethylindodicarbocyanine perchlorate (DiD), 3,3'-dioctadecyloxacarbocyanine perchlorate (DiO), and Bacmam 2.0 Cell lights Nuclear-GFP baculovirus, were purchased from Molecular Probes by Life Technologies (Grand Island, NY) in the form of DiD and DiO Vybrant cell labelling solutions, and BacMam Cell Light transfection reagent. Paraformaldehyde (PFA) solution (32%) was purchased from Electron Microscopy Supplies (Hatfield, PA). A 6.1 μm spherical polystyrene AFM probe was purchased from NanoAndMore (Lady's Island, SC). The anti-fade reagent used was supplied by the Molecular Cytology core facility at Memorial Sloan Kettering Cancer Center.

2.2 Cell culture and fluorescent labelling

Cell culture was as earlier described^{1,14,15,26}. Human dermal fibroblasts were cultured on gelatin coated surfaces (0.1% in PBS) in DMEM- α (15% FCS). MC cell lines were: melanoma MM200-B12 cultured in DMEM- α (10% FCS); and osteosarcoma cells SAOS-2 in M199 (10% FCS).

Labelling solutions of DiD for fibroblasts (1mM) and DiO for MC (2mM) were applied to cells for 30 min in the case of DiD, and 1h for DiO. Monolayers were washed prior to overnight culture and further washing before co-culture. In some experiments, MM200-B12 were transfected with green fluorescent protein (GFP) expressing baculovirus.

2.3 Co-culture conditions

Co-cultures were on gelatin (0.1% in PBS) coated surfaces with Fibroblasts seeded from 1 to 2 x 10⁴ cells per cm² into either 25cm² AFM culture plates²⁶, or culture well coverslips, and allowed to adhere overnight before labelling. MC were seeded at near confluence in either 25 cm² flasks or 6 well culture plates prior to labeling. MC were then harvested with trypsin-EDTA and seeded over fibroblasts in DMEM- α with BSA (4%) at 4 x 10⁴ cells per cm² for up to 24 h co-culture.

2.4 Time-lapse CLSM

Eight separate visual fields of fibroblasts co-cultured with GFP labelled MM200-B12 were recorded for 25 h at 3 min intervals, representing 1.13 mm² culture surface area. Nine further separate visual fields of DiO pre-labelled MM200-B12 were recorded for 8 h 15 min at 5 min intervals and at slightly higher magnification, representing 0.76 mm² culture surface area. Monolayers were fixed with paraformaldehyde after co-culture. CLSM was by a Zeiss LSM 5Live line-scanning confocal microscope.

2.5 Assumptions made in mathematical modelling

CPP was described mathematically for a simple two chamber hydrodynamic system joined by a cylindrical connector, each chamber representing either Donor Cell A, or Receptor Cell B, and the cylindrical connector representing a cell-projection from Cell A. In absence of more detailed temporal observations, we assume a constant rate for retraction of cell-projections.

Calculations were based on the well described Hagen-Poiseuille relationships, where resistance to flow in a cylindrical tube (ρ) is given by equation (1), and the flow rate (Q) of a Newtonian fluid of viscosity (η) through a cylindrical tube of length (L) with radius (r), due to a pressure difference (ΔP) as per equation (2)²⁷.

$$\rho = \frac{8 \eta}{\pi \cdot r^4} \quad (1)$$

$$Q = \frac{\Delta P}{\rho \cdot L} = \frac{\Delta P \cdot \pi \cdot r^4}{8 \eta \cdot L} \quad (2)$$

Because the fluid volumes exchanged between cells are very small, it was reasonable to assume negligible bulk modulus effect, and the cytoplasm exchanged between cells was assumed to behave as an incompressible Newtonian fluid. Pascal's law predicts that any pressure change within

a confined Newtonian fluid is transmitted throughout the fluid such that the change is the same throughout²⁸. Pascal's law thus renders modeling of fluid flow in the current study independent of non-topological geometric details, so that bends and connection to blind-ending branches, should have little or no effect on quantitative results.

Notably, the hydraulic system modelled is not confined, but consists instead of two 'open' halves, each of which operates against a separate constant reaction force term in the form of a reaction pressure, F , (being F_A and F_B for Donor and Receptor cells respectively). Hence each half has a separate ΔP (ΔP_A and ΔP_B for Donor and Receptor Cells respectively), as also demanded by Pascal's law²⁸.

A central component of the CPP mechanism is the resistance to cytoplasmic flow into each of the cells. Whereas the simplest assumption is that this is elastic in nature, initial investigation demonstrated that this could not explain the experimental data. Cytoplasm comprises a mixture of viscous cytosol, organelles and the cytoskeleton, and behaves as a viscoplastic material, which is elastic as applied stress increases from zero until a yield point, and in which viscoelastic flow occurs beyond the yield point²⁹.

The yield point involves the breakage of structural bonds to allow cytosol with its burden of organelles to force its way through the structure, as viscoelastic flow in the presence of an applied force. Contrasting strongly with this, is the simple viscous flow that we assume for contents of cell-projections, on basis that the internal structure of cell-projections is significantly more simple compared with that of the cell body.

To avoid unjustifiable elaboration, we assume that the cells are described by a Bingham plastic model where the stress – strain rate characteristic consists of a single straight line segment. Because the flow from the projection into the cell spreads out into the larger cell body, we assume that the apparent viscosity is essentially zero, i.e. that the slope of the line segment is approximately zero and can be neglected.

Consequently the effect of each cell on the flow from the projection can be accounted for by a single force term equivalent to the yield point (P^Y), of the cell cytoplasm. These force terms are the reaction pressures F_A and F_B . The yield point occurs when the deformation of the material under stress reaches a critical level and this critical deformation of the cell's cytoplasm for a particular stress level is inversely proportional to the Young's modulus of the material. Assuming that this critical deformation is approximately the same for both cells, the yield point can be assumed to be proportional to the stiffness of the cell, S , as measured by AFM. If Z is the constant of proportionality then $P_A^Y = ZS_A$, and $P_B^Y = ZS_B$.

It seems reasonable to assume only modest effect of the simplifying assumptions outlined above, in diverging the calculated estimations made in the current study, from events in-vivo.

2.6 Combined atomic force and fluorescence microscopy

Paraformaldehyde fixed monolayers were stored in PBS at 4° C for combined fluorescence-AFM recordings of randomly selected cells²⁶. An Asylum Research MFP-3D-BIO atomic force microscope coupled with a Zeis Axio Observer A1 fluorescence microscope was used. Bright field and fluorescence images for both DiO and DiD channels were recorded prior to AFM scanning. A 1 μ m AFM spherical polystyrene probe was used to record 16 x 16 points of force curves over 50 μ m x 50 μ m areas. Asylum Research, Software Version IX Young's modulus for each point by the Hertz model^{26,30}. Height maps, bright field and fluorescence images were compared to localize discrete AFM measurement points to individual cells, and stiffness fingerprints were prepared²⁶.

2.7 Morphometric analysis and cell stiffness analysis

ImageJ open source software (<http://imagej.net/Contributors>) was used to segment and analyze fluorescence images of individual SAOS-2 and fibroblasts. Cell surface profile area was determined, while both Red and green fluorescence was summated for each cell. Fluorescence intensity in both fluorescence channels was expressed in 'Fluorescence Units' (summated fluorescence / surface profile area). Both fibroblasts and SAOS-2 were designated as belonging to one of two groups, being 'high' or 'low' labelling from the opposing cell type. Median AFM stiffness was determined for individual cells, while stiffness fingerprints were also made of cells according

to group to address sampling limitations as earlier described²⁶. Prism 6.0e software (GraphPad Software Inc, La Jolla, CA) was used for statistical analysis.

2.8 Computer simulation of cytoplasmic and fluorescence transfer between fibroblast and SAOS-2 populations by CPP

Estimated cumulative distribution functions (ECDF) were developed in MATLAB (MATLAB by MathWorks Inc) from experimental median cell stiffness and fluorescence data (MATLAB Scripts provided in Supplementary Information). ECDFs were then used to generate simulated populations of cells with distributions for stiffness and fluorescence closely approximating those of experimental data. This method was used to generate 5100 donor fibroblasts, 5100 donor SAOS-2, 5000 recipient SAOS-2, and 5000 recipient fibroblasts (Supplementary Fig. S1).

Co-culture simulations were in MATLAB of random interactions between simulated donor and receptor cells, making random selection of values from lists of variables used to calculate CPP. Values loaded into these lists had distributions bounded by target minimum and maximum values, while target minima and maxima were established at the start of each simulation. Variables modelled in this way were: the number of Donor Cells A each Receptor Cell B could interact with; the number of transfer events each Receptor Cell B could have with each Donor Cell A; the flow rate (U) for each transfer event; the length at time 0 (L_0) of each cell-projection; the radius (r) of each cell-projection; and the viscosity of cytoplasm (η). Values for these parameters, were inferred on basis of CLSM observations, with exception of viscosity, which was taken from the literature^{31,32}. The only exception to this was for the time permitted for each transfer event, the maximum of which is defined by L_0/U , and random choice of time was made from a pre-determined proportionate range between 0 and L_0/U . MATLAB script for simulations is provided in Supplementary Information.

Average SAOS-2 and fibroblast cell height was determined from AFM data (3.89×10^{-6} m and 2.36×10^{-6} m respectively), while average SAOS-2 and fibroblast cell surface area (1.53×10^{-9} m² and 5.34×10^{-9} m² respectively) was by image analysis from separate experiments, and these data were used to calculate fluorescence from volume transfers.

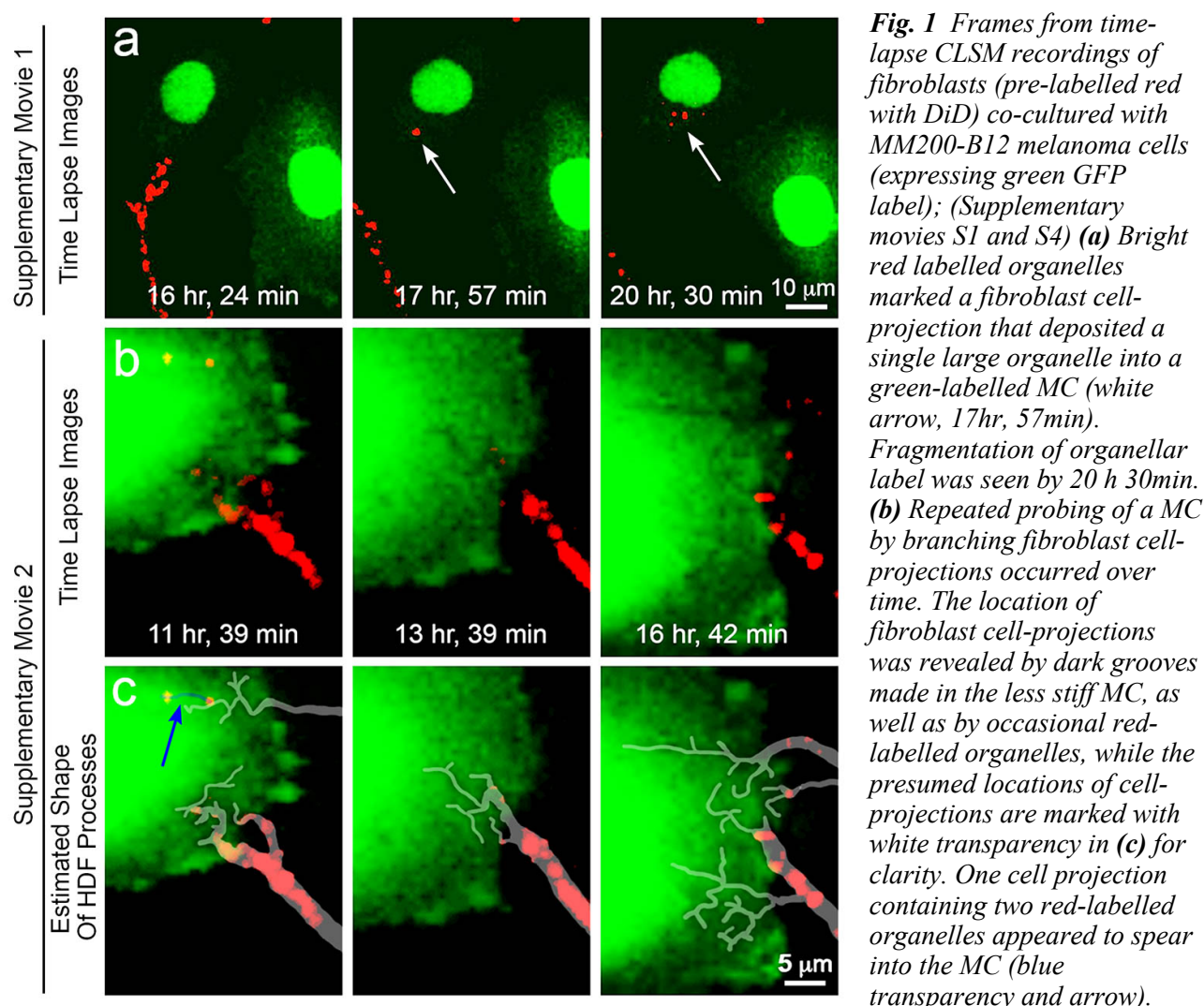
Volume and fluorescence transfers for each simulated cell pairing were determined, and summated simulation results compared with experimental results. Maximal pressure generated during individual simulated CPP events was also recorded. Distributions of input variables as well as simulation outcomes were plotted in histograms (Supplementary Figs S2 and S3 show results of simulations approximating experimental observations). Data were analyzed using PRISM 7 (GraphPad Software Inc), and Mann Whitney U Tests where appropriate.

3 Results

3.1 Time-lapse CLSM indicated exchange of cytoplasmic organelles between cells was via cell-projections with the appearance of branching filopodia and lamellipodia

3.1.1 Transfer of organelles between fibroblasts and MC were frequently seen in time-lapse recordings

Obvious acquisition of DiD (red) labelled fibroblast organelles was observed in 11 out of 106 DiO (green) pre-labelled MC, during 8 h 15 min co-culture, and 7 out of 71 GFP (green) pre-labelled MC during 25 h co-culture. From this, a total of 18 MC were observed receiving fibroblast organelles, studying 33 h 15 min of time-lapse recordings (Figs. 1a, 2a,b; Supplementary movies S1 and S2, Legends for movies in Supplementary Information). Only a single occasion was observed, where DiO (green) labelled organelles were transferred from a single MC to a fibroblast, via broad cell-projection structures with the appearance of lamellipodia (Supplementary movie S3, Legend in Supplementary Information). Although occasional large prominent fibroblast organelles were accepted by MC (Fig. 1a; Supplementary movie S1, Legend for movie in Supplementary Information), most exchange was of smaller organelles, and this was most readily seen when MC were labeled with DiO (green) (Fig. 2; Supplementary movie S2, Legend for movie in Supplementary Information). Note that organellar labelling was used for time-lapse microscopy, because punctate organellar fluorescence is advantageous for tracking the movement of otherwise diffuse cytoplasm.



3.1.2 Fine cell-projections transferring fibroblast organelles were evidenced by the grooves they formed in MC

Because fibroblast cell-projections transferring organelles to MC were largely transparent by CLSM, they could not be resolved to a high degree of accuracy. However, the shape and location of these transparent fibroblast cell-projections could be inferred by careful examination of CLSM z-stack images in time-lapse movies, where deep grooves were seen in the surfaces of MC (Figs. 1b,c; 2c,d). We interpret these grooves as having been formed by fibroblast cell-projections with high stiffness, compared with the MC they deeply indented. Confirming our interpretation for the location of these transparent fibroblast cell-projections, was the presence of occasional scattered DiD labeled fibroblast organelles within the grooves (Fig. 1b,c; Fig. 2c,d; Supplementary movies S2 and S4, Legends for movies in Supplementary Information).

Fibroblast cell-projections indenting MC, appeared as tree-like branching networks that terminated in long filopodia-like extensions (Figs. 1b,c, 2c,d; Supplementary Information movies S2 and S4, legends for movies in Supplementary Information). While the overall shape of fibroblast cell-projections was stable over time, the fine terminal branches were labile in shape and varied within the 3 and 5 min intervals between time-lapse frames (Figs. 1b,c; 2c,d; Supplementary Information movies S2 and S4, Legends for movies in Supplementary Information). Supporting our interpretation for the presence of fibroblast cell-projections in MC grooves, was that the MC grooves ceased to be apparent when large fibroblast cell-projections became sufficiently distant, as seen comparing Fig. 2c recorded at 7 h 10 min, with Fig. 2c recorded at 8 h 5 min.

Cell-projections alternately probed and retracted from individual receptor cells, and episodes of organellar transfer appeared to coincide with retraction events (Supplementary Information movies S1 to S3, Legends in Supplementary Information).

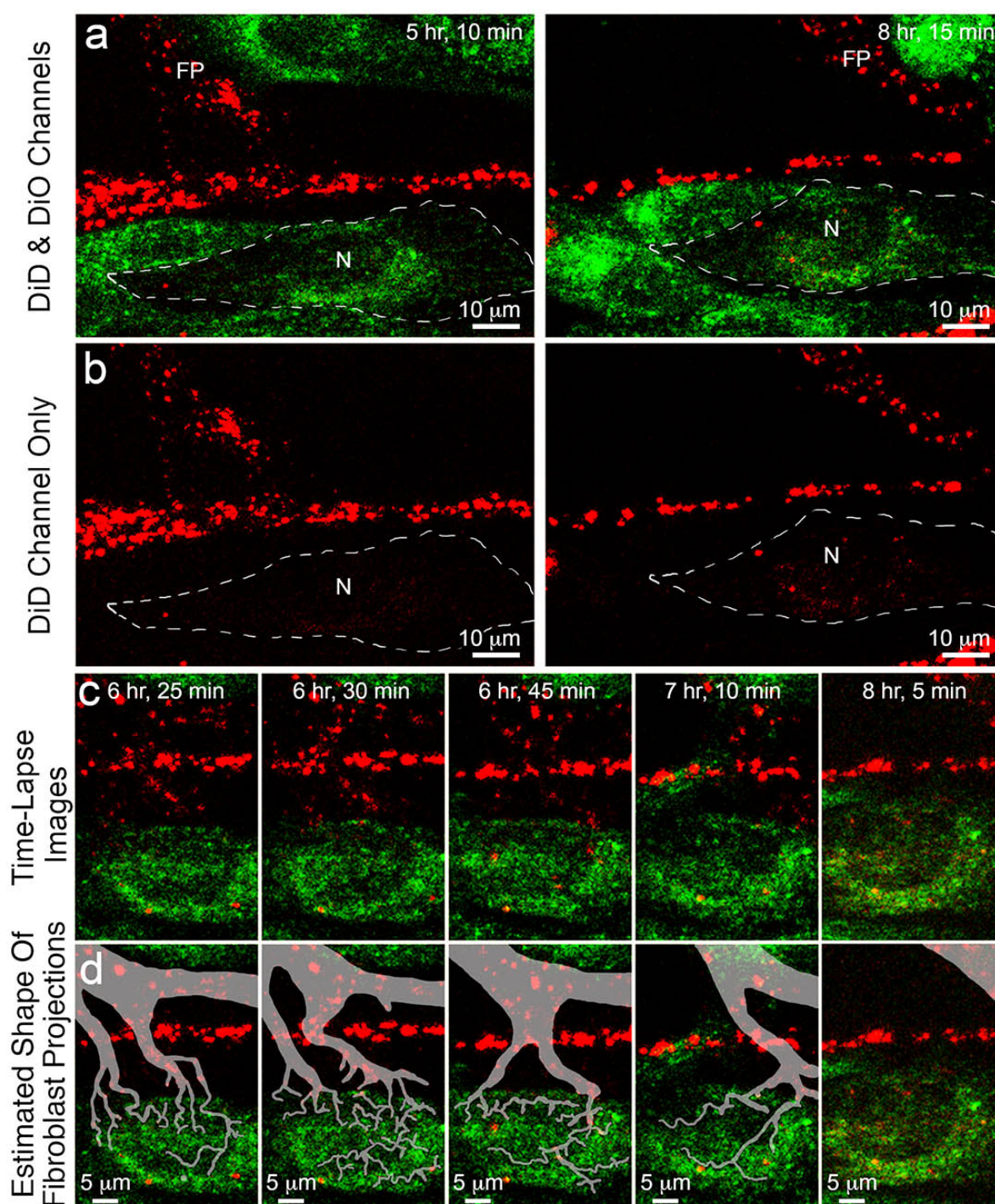


Fig. 2 Frames from a time-lapse CLSM recording of fibroblasts (pre-labelled with DiD-red) co-cultured with MM200-B12 melanoma cells (pre-labelled with DiO-green); (Supplementary Movie S2). **(a, b)** A MC (white dashed outline) received appreciable red fibroblast organellar labelling between 5 h 10min and 8 h 15min, most clearly seen when the green channel is excluded **(b)**. **(c)** This was from a broad fibroblast cell-projection (FP) that swept past the MC, indenting and grooving the recipient cell with numerous smaller branching cell-projections, no longer seen by 8 h 5min. **(d)** White transparency marks the presumed location of fibroblast cell-projections grooving the MC.

3.1.3 TNT, exosomes, fragmenting budding and non-specific label transfer did not account for observations

Occasional TNT were observed, but made minimal contribution to the observed transfers. Similarly, fragments of fibroblasts were sometimes seen, but were clearly phagocytosed by cells. Also, the highly localized transfer of label to discrete cells together with evident transfer via discrete cell-projections, excluded a significant role for exosomes or other shed membrane vesicles.

Further, lack of label transfer between many cells in intimate physical contact, spoke against a role for passive label diffusion (Figs. 1, 2; Supplementary Figs. S4 to S6). It was evident from time-lapse movies, that organellar transfer from donor to recipient cells could only occur if there were transient cytoplasmic continuities through fused plasma membrane windows joining adjacent cells, similar to that established for TNT, but in this instance occurring via cell-projections, often in the size range of filopodia.

We considered the possibility that fragments of donor cells could have been ‘torn off’ during cell-projection retraction, and then internalized by phagocytosis. However, such a mechanism would require both: fragmenting budding of cell-projections, and the formation of recipient cell surface spikes drawn out by retracting cell-projections; neither of which were ever seen during transfer events. Also, transferred organelles were always clearly intracellular, inconsistent with a ‘budding and phagocytosis’ mechanism, so this seemed excluded by our observations.

Lacking high resolution images of the cell-projections through which transfer occurred, but having nonetheless observed that fine structures transferred cytoplasmic organelles during episodes of cell-projection retraction, we hypothesized CPP as a mechanism to account for our observations.

3.2 The CPP hypothesis

To account for our data (3.1), we hypothesize CPP as a hydrodynamic pumping mechanism. On first principles, a transient increase in hydrodynamic pressure must occur within a retracting cell-projection, in order to return cytoplasm to the cell body. Also, and consistent with the observed formation of TNT, we suggest the presence of occasional cytoplasmic continuities between potential donor cell projections and recipient cells. Should the presence of such a cytoplasmic continuity coincide with retraction of a cell-projection, raised pressure within the cell projection partially equilibrates by cytoplasmic flow into a recipient cell. Because fluid flow is preferential towards least resistance, the extent of CPP is influenced by the relative stiffness of individual donor and recipient cells (Fig. 3a).

3.2 Mathematical model for CPP

3.2.1 General features of the model

Fig. 3b shows the simple two chamber system used to model CPP mathematically, relating a constant rate of retraction of the cell projection (U), to pressure (ΔP_A and ΔP_B) for both chambers from fluid escaping the shortening cell-projection.

Only flow into Receptor Cell B (Q_B) was calculated in the current study, since it is only Q_B which will deliver cytoplasm to the opposing cell (Fig. 3b). Also, since maximum pressure is located within of the retracting cell-projection at position O (described below, Fig. 3ciii), there is no actual cytoplasmic flow at O which acts as an effective 'syringe plunger' for flow in both cell directions. ΔP is exhausted upon complete retraction, thus limiting the total possible volume of flow to that of the cell-projection.

3.2.2 Modification of the Hagen-Poiseuille equation accommodating differences in cell stiffness

Distribution of fluid during retraction of the cell-projection in Fig. 3a,b is influenced by the relationship between stiffness of Donor Cell A (S_A) and Receptor Cell B (S_B), and this requires modification of the relationships described in equations (1 and 2) for calculation of that portion of total flow distributed to Receptor Cell B (Q_B).

Fig. 3ci shows a cylindrical tube of known length ($L(t)$) at time (t) as measured from '0' at it's origin which is closed and marked to the left, and in which there is contraction at a constant rate (U), as indicated in equation (3).

$$U = \frac{L(t)}{dt} \quad (3)$$

The tube contains a Newtonian fluid, and is divided into n cylinders of equivalent length (Δx) as shown in equation (4), indexed from $n=1$ to n (Fig. 3cii).

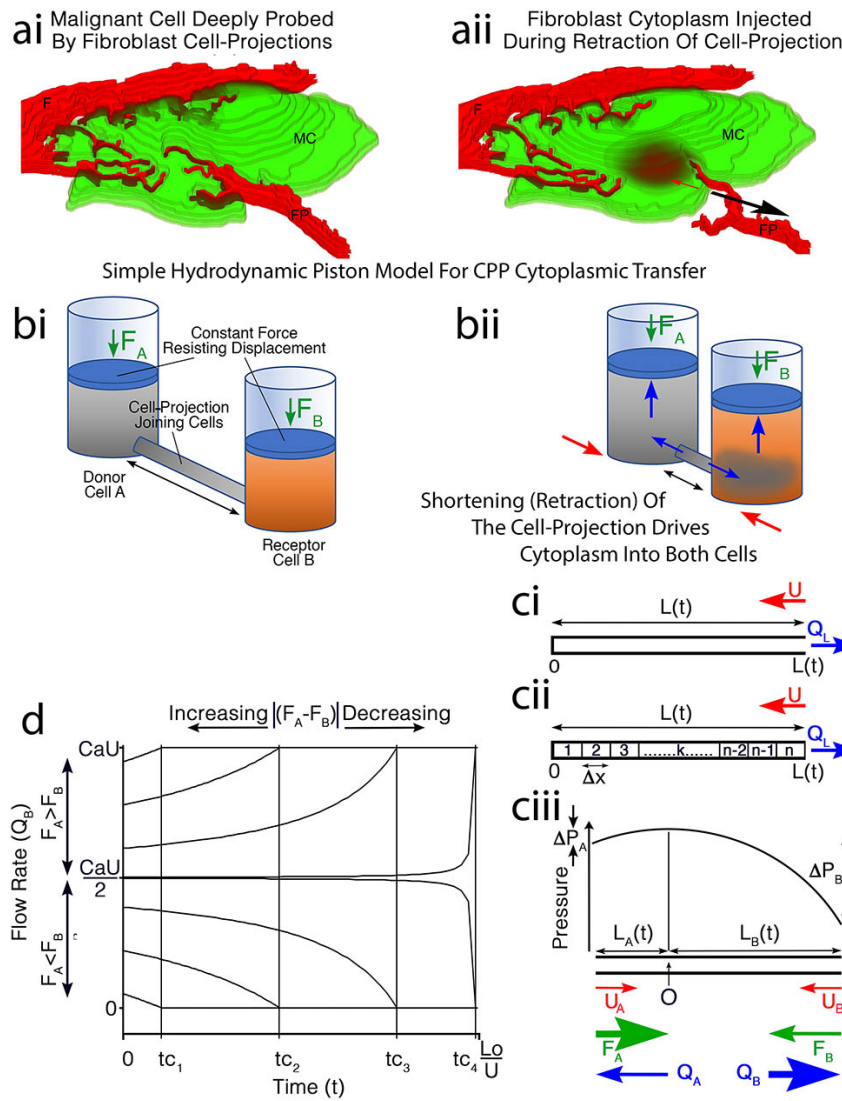


Fig. 3 The cell-projection pumping (CPP) hypothesis for transfer of cytoplasm. **(a)** A cartoon is drawn from a confocal image containing a MC deeply grooved by fibroblast (F) cell-projections (FP). **(aai)** If there is a transient inter-cellular cytoplasmic continuity, retraction of the cell-projection (black arrow) drives some fibroblast cytoplasm into the MC (red arrow). **(bi)** This is modelled with piston-cylinders connected by a cylindrical tube (black arrow) containing a Newtonian fluid from the 'Donor Cell'. **(bii)** Shortening of the tube (red arrows) mimics cell-projection retraction, driving Donor Cell contents into both 'Donor' and 'Receptor Cells' (blue arrows), once the yield points against constant forces of resistance proportionate to cell stiffness (F_A , F_B , green arrows) are reached. **(ci)** Consider a close-ended tube with length $L(t)$ contracting at constant rate U (red arrow), and generating a flow rate of a fluid within the tube of Q_L (blue arrow). **(cii)** Dividing the tube into n

cylinders of Δx length, with Δx approaching zero, relates $L(t)$ to pressure and Q_L . **(ciii)** Two such tubes of lengths $L_A(t)$ and $L_B(t)$ are opened and joined at their origins (O), contracting at U_A and U_B ($U_A + U_B = U$) (red arrows), with flow (Q_A and Q_B , blue arrows) against constant forces (F_A and F_B , green arrows) due to and proportionate to cell stiffness (S_A and S_B), such that $F = ZS$ where Z is a constant. Pressure is maximal at P_0 , and equals F_A and F_B at the open ends, establishing ΔP_A and ΔP_B . Where $F_A > F_B$ ($S_A > S_B$), $L_A(t) < L_B(t)$ and $Q_A < Q_B$; this reverses when $F_A < F_B$ ($S_A < S_B$); while when $F_A = F_B$ ($S_A = S_B$), $Q_A = Q_B$. **(d)** Q_B is plotted over time for retraction to extinction of a cell-projection. Notably, when $F_A > F_B$ ($S_A > S_B$), there is a time (tc) when $L_A = 0$, $Q_A = 0$, and remaining flow is $Q_B = CaU$, where Ca = tube cross-sectional area. When $F_A < F_B$ ($S_A < S_B$), $L_B = 0$ at tc , so that $Q_B = 0$, and remaining flow is Q_A . Decreasing $F_A - F_B$ ($S_A - S_B$) increases tc .

$$\Delta x = \frac{L(t)}{n} \quad (4)$$

Because the tube undergoes a constant contraction, each cylinder also contracts by $U\Delta t/n$ to displace a volume of fluid (ΔV) as in equation (5), where Ca is the cross-sectional area of the tube.

$$\Delta V = \frac{Ca \cdot U(\Delta t)}{n} \quad (5)$$

In this way, each cylinder donates an equivalent volume (ΔV) and flow rate increment ($\Delta q = \Delta V/\Delta t$), to the total flow rate of the cylinder as in equation (6), substituting for n from equation (4).

$$\Delta q = \frac{Ca \cdot U}{n} = \frac{Ca \cdot U \cdot \Delta x}{L(t)} \quad (6)$$

Rearrangement of equation (6) gives equation (7).

$$\frac{\Delta q}{\Delta x} = \frac{Ca \cdot U}{L(t)} \quad (7)$$

As $n \rightarrow \infty$, $\Delta x \rightarrow 0$, so that the flow rate at x , ($Q(x)$), is given by equation (8).

$$Q(x) = \int_0^x \frac{Ca \cdot U}{L(t)} dx = \frac{Ca \cdot U \cdot x}{L(t)} \quad (8)$$

Note that the flow rate at the end of the tube where $x=L(t)$ is CaU as expected (Fig. 3cii).

Let ρ be the resistance per unit length as given in equation (1), so that the resistance offered by any given small cylinder comprising the cell-projection (ΔR) is given by equation (9), and the pressure drop across the cylinder ($\Delta P_{\Delta x}$) is given by equation (10) as per equations (2 and 6).

$$\Delta R = \rho \cdot \Delta x \quad (9)$$

$$\Delta P_{\Delta x} = \Delta q \cdot \Delta R = \frac{Ca \cdot U}{n} \cdot \rho \cdot \Delta x \quad (10)$$

The pressure drop at any given cylinder k and $L=x$ is given by equation (13), which can be rearranged to equation (14).

$$\Delta P_X = \frac{k \cdot Ca \cdot U}{n} \cdot \rho \cdot \Delta x \quad (13)$$

$$\frac{\Delta P_X}{\Delta x} = \frac{k \cdot Ca \cdot U \cdot \rho}{n} \quad (14)$$

Substituting for $1/n$ from equation (4), and recognizing that $x = k\Delta x$ gives equation (13).

$$\frac{\Delta P}{\Delta x} = \frac{Ca \cdot U \cdot \rho \cdot k \cdot \Delta x}{L(t)} = \frac{Ca \cdot U \cdot \rho \cdot x}{L(t)} \quad (13)$$

Allowing $\Delta x \rightarrow 0$, gives the expressions in equation (14).

$$\frac{\Delta P}{\Delta x} \rightarrow \frac{dP(x)}{dx} = \frac{Ca \cdot U \cdot \rho \cdot x}{L(t)} \quad (14)$$

From this, the pressure drop $P(x)$ at x , is given as expressions in equation (15).

$$P(x) = \int_0^x \frac{Ca \cdot U \cdot \rho \cdot x}{L(t)} dx = \frac{Ca \cdot U \cdot \rho \cdot x^2}{2 \cdot L(t)} \quad (15)$$

Consider the above outlined system now duplicated, and one of these elements to be rotated so that the two tubes now abut end to end, with the origin $x=0$ being identical for both. This now represents a cell-projection joining Donor Cell A 'to the left', with Receptor Cell B positioned 'to the right'. The origin represents a point in the cell-projection (P_o) where during contraction of the cell-projection, there is maximum pressure and no flow, the origin functioning as an effective 'syringe stop' for flow in both directions. The length of tube between the origin and Donor Cell A is L_A , and that to Receptor Cell B is L_B (Fig. 3ciii), giving equation (16) for length at time t .

$$L(t) = L_A(t) + L_B(t) \quad (16)$$

The tube is open to Cells A and B, and flow out of the tube in both directions is resisted by constant reaction pressures F_A and F_B in Cells A and B respectively (Fig. 3ciii). These reaction pressures are equal to the yield points P_A^Y and P_B^Y which are proportionate but not identical to the measured median cell stiffness of the Donor and Receptor cells (S_A and S_B), so that it may be helpful to read 'S' for 'F' when making reference to Figs. 3b,c.

Noting that U is constant, equation (16) gives equation (17) following simplification, where: $U = L/t$, $U_A = L_A/t$, and $U_B = L_B/t$.

$$U = U_A + U_B \quad (17)$$

The relationships in equation (18) follow from the above.

$$\frac{U_A}{U} = \frac{L_A(t)}{L(t)} \quad \frac{U_B}{U} = \frac{L_B(t)}{L(t)} \quad (18)$$

If $P_{max}(t)$ is the pressure at the origin (O), then from equation (15), the pressure at x_B going to the right (P_R) is given by equations (19), ultimately reaching and being balanced by the hydrodynamic force resisting flow by Cell B (F_B) to the right, with pressure at x_A going left (P_L) reaching the hydrodynamic force resisting flow by Cell A (F_A) to the left (equation (19)), as illustrated in Fig. 3ciii.

$$P_R(x) = P_{max}(t) - \frac{Ca \cdot U_B \cdot \rho \cdot x_B^2}{2 \cdot L_B(t)} \quad P_L(x) = P_{max}(t) - \frac{Ca \cdot U_A \cdot \rho \cdot x_A^2}{2 \cdot L_A(t)} \quad (19)$$

Since $L_A = x_A$, and $L_B = x_B$, equations (19) simplify to equations (20).

$$P_R(x) = P_{max}(t) - \frac{Ca \cdot U_B \cdot \rho \cdot L_B(t)}{2} = F_B \quad P_L(x) = P_{max}(t) - \frac{Ca \cdot U_A \cdot \rho \cdot L_A(t)}{2} = F_A \quad (20)$$

Rearrangement of equations (20) gives equation (21).

$$F_A + \frac{Ca \cdot U_A \cdot \rho \cdot L_A(t)}{2} = F_B + \frac{Ca \cdot U_B \cdot \rho \cdot L_B(t)}{2} \quad (21)$$

Substituting for L_A from equation (16) gives equation (22).

$$F_A + \frac{Ca \cdot U_A \cdot \rho \cdot (L(t) - L_B(t))}{2} = F_B + \frac{Ca \cdot U_B \cdot \rho \cdot L_B(t)}{2} \quad (22)$$

Substitution for: U_B from equation (17); U_A/U from equation (18); and L_A from equation (16), gives equation (23) for L_B .

$$L_B(t) = \frac{F_A - F_B}{Ca \cdot U \cdot \rho} + \frac{L(t)}{2} \quad (23)$$

The algebraic relationships leading to equation (23) apply equally to generate equation (24).

$$L_A(t) = \frac{F_B - F_A}{Ca \cdot U \cdot \rho} + \frac{L(t)}{2} \quad (24)$$

From equations (23 and 24), when $F_A = F_B$, then $L_A(t) = L_B(t) = L(t)/2$, and both cells receive equivalent flow as expected from symmetry of the system. When $F_A > F_B$, a time is reached when $L_A(t)$ reaches 0 and all remaining flow is to the right, and Receptor Cell B receives more flow than Cell Donor Cell A (Fig. 3ciii), while the reverse applies when $F_A < F_B$.

Note that in equations (20) $P_{max}(t)$ is a decreasing function of time so that when $L_A(t) = 0$, for $F_A > F_B$, $P_{max}(t)$ is at the yield point of cell A P_A^Y . As $P_{max}(t)$ decreases further the cell A

cytoplasm enters the elastic regime of the Bingham plastic model and F_A decreases so as to track $P_{max}(t)$ in accordance with Newton's Third Law.

Equation (25) follows from equation (8).

$$Q_B = \frac{Ca \cdot U \cdot L_B(t)}{L(t)} \quad (25)$$

To establish the total flow transferred to Receptor Cell B ($Q_B(t)$), $L_B(t)$ from equation (23) is substituted into equation (25), which with simplification gives equation (26).

$$Q_B = \frac{F_A - F_B}{\rho \cdot L(t)} + \frac{Ca \cdot U}{2} \quad (26)$$

Because U is constant, $L(t)$ is given by equation (27), and substitution for $L(t)$ in equation (26) gives equation (28).

$$L(t) = L_0 - U \cdot t \quad (27)$$

$$Q_B = \frac{F_A - F_B}{\rho \cdot (L_0 - U \cdot t)} + \frac{Ca \cdot U}{2} \quad (28)$$

Note that equation (28) can only apply while $(F_A - F_B)/\rho(L_0 - Ut) \leq CaU/2$, because at this point $L_A = 0$ and $L_B = L$ where $S_A > S_B$, with all flow being to the right into Receptor Cell B at a rate of $Q_B = CU$; while where $S_A < S_B$, $L_B = 0$ and $L_A = L$ and all remaining flow is to the left into Donor Cell A. Let the time at which this occurs be tc to give equation (29).

$$\frac{F_A - F_B}{\rho \cdot (L_0 - U \cdot tc)} = \frac{Ca \cdot U}{2} \quad (29)$$

Expansion, rearrangement and simplification of equation (29), gives equation (30) for tc , where the absolute value of second term on the right is required to accommodate occasions when $F_A < F_B$.

$$tc = \frac{L_0}{U} - \left| \frac{2(F_A - F_B)}{Ca \cdot \rho \cdot U^2} \right| \quad (30)$$

Fig. 3d is a graphical representation of Q_B from $t = 0$ to $t = L_0/U$ at which time $L_B = 0$ and no further flow Q_B is possible. When $F_A > F_B$, equation (28) for Q_B applies for $t \leq tc$, and $Q_B = CaU$ for $tc < t < L_0/U$. Increasing values of $(F_A - F_B)$ reduce tc , while as $(F_A - F_B)$ approaches 0, tc approaches L_0/U and Q_B approximates $CaU/2$ from above for increasing time when $F_A > F_B$, and from below when $F_A < F_B$. Also, when $F_A < F_B$, equation (28) predicts that Q_B approaches 0 as t approaches tc , after which Q_B remains 0 due to exhaustion of L_B to 0 at tc .

3.2.3 Calculation of volumes transferred

Volumes transferred can be calculated by integration of curves such as show in Fig. 3d. Let the total volume transferred to Receptor Cell B be V_B .

Where $F_A > F_B$, the relationships outlined above determine $V_B(t)$ as per equation (31).

$$V_B(t) = \int_0^{tc} \left(\frac{Ca \cdot U}{2} + \frac{F_A - F_B}{\rho \cdot (L_0 - U \cdot t)} \right) dt + \int_{tc}^{L_0/U} (Ca \cdot U) dt \quad (31)$$

Similarly, where $F_A < F_B$, $V_B(t)$ is given by equation (32).

$$V_B(t) = \int_0^{tc} \left(\frac{Ca \cdot U}{2} + \frac{F_A - F_B}{\rho \cdot (L_0 - U \cdot t)} \right) dt \quad (32)$$

Also, where $F_A = F_B$, $V_B(t)$ is given by equation (33).

$$V_B(t) = \int_0^{L_0/U} \left(\frac{Ca \cdot U}{2} \right) dt \quad (33)$$

To aid integration in equations (31 and 32), define $w(t)$ as in equation (34), such that when $t = 0$, $w = L_0$; and when $t = tc$, $w = L_0 - Utc$.

$$w(t) = L_0 - U \cdot t \quad (34)$$

Differentiating equation (34) gives equation (35).

$$dw = -U \cdot dt \quad (35)$$

From this, the second term in equations (31 and 32) can be expressed and integrated with regard to w as in equation (36), where $\ln(w)$ is the natural logarithm of w . Substitution of equation (34) into equation (36) gives the expression in equation (37).

$$-\frac{1}{U} \int_{L_0}^{(L_0 - U \cdot tc)} \left(\frac{F_A - F_B}{\rho \cdot w} \right) dw = -\frac{F_A - F_B}{\rho \cdot U} \cdot \ln(w) \Big|_{L_0}^{L_0 - tc \cdot U} \quad (36)$$

$$= -\frac{F_A - F_B}{\rho \cdot U} \cdot \begin{cases} \ln\left(\frac{L_0 - U \cdot t}{L_0}\right), & \text{if } t \leq tc \\ \ln\left(\frac{L_0 - U \cdot tc}{L_0}\right), & \text{if } t > tc \end{cases} \quad (37)$$

From equation (37), the integral of $V_B(t)$ for $0 < t < tc$ in equations (31 and 32) is as in equation (38).

$$\frac{Ca \cdot U \cdot t}{2} - \frac{F_A - F_B}{\rho \cdot U} \cdot \ln\left(\frac{L_0 - U \cdot t}{L_0}\right) \quad (38)$$

Combining the result of equation (38) with equations (31, 32, 33) provides equations (39 to 42) used to determine V_B for all conditions tested in the current study, where: tm is the time at which any given contraction event ceases; and Z is a constant correcting for the assumed linear relationship between median cell stiffness and both F_A and F_B , such that $ZS_A = F_A$, and $ZS_B = F_B$. Maximum pressure drop was calculated from equation (11).

Where $S_A > S_B$, and tm is $\leq tc$, V_B is calculated by equation (39).

$$V_B = \frac{Ca \cdot U \cdot tm}{2} - \frac{Z \cdot (S_A - S_B)}{\rho \cdot U} \cdot \ln\left(\frac{L_0 - U \cdot tm}{L_0}\right) \quad (39)$$

Where $S_A > S_B$, and tm is $> tc$, V_B is calculated by equation (40), noting that tm cannot exceed L_0/U .

$$V_B = \frac{Ca \cdot U \cdot tc}{2} - \frac{Z \cdot (S_A - S_B)}{\rho \cdot U} \cdot \ln\left(\frac{L_0 - U \cdot tc}{L_0}\right) + Ca \cdot U \cdot (tm - tc) \quad (40)$$

Where $S_A < S_B$, and tm is $\leq tc$, V_B is calculated by equation (39).

Where $S_A < S_B$, and tm is $> tc$, V_B is calculated by equation (41).

$$V_B = \frac{Ca \cdot U \cdot tc}{2} - \frac{Z \cdot (S_A - S_B)}{\rho \cdot U} \cdot \ln\left(\frac{L_0 - U \cdot tc}{L_0}\right) \quad (41)$$

Where $S_A = S_B$, V_B is calculated by equation (42).

$$V_B = \frac{Ca \cdot U \cdot tm}{2} \quad (42)$$

2.3.4 Testable predictions from the mathematical model

The relationships illustrated in Fig. 3d permit predictions that could be tested in experimental co-cultures, and also by numerical simulations. Since tc decreases with increasing $|F_A - F_B|$ to maximize flow for positive values of $(F_A - F_B)$, and minimize flow for negative values of $(F_A - F_B)$; an inverse correlation was predicted between recipient cell stiffness and CPP uptake of donor cell cytoplasm. Also, preferential CPP transfer of cytoplasm was expected from populations of cells with high stiffness, towards cell populations with low cell stiffness, given otherwise identical CPP conditions.

3.3 Experimental measurement of cell stiffness and fluorescence in co-cultured cells satisfied predictions of the mathematical model.

Fluorescence microscopy of a co-culture of fibroblasts with SAOS-2, revealed the most evident transfer of fluorescent label was from fibroblasts to SAOS-2, with less obvious fluorescence transfer from SAOS-2 to fibroblasts. Fluorescence and atomic force microscopy (AFM) stiffness data for these cells are shown in Fig. 4. Although micro-domains varied greatly in stiffness across the surfaces of individual cells, stiffness fingerprints clearly demonstrated that fibroblasts were stiffer and had lower cell height compared with SAOS-2 (Mann Whitney U Test, $p < 0.0001$).

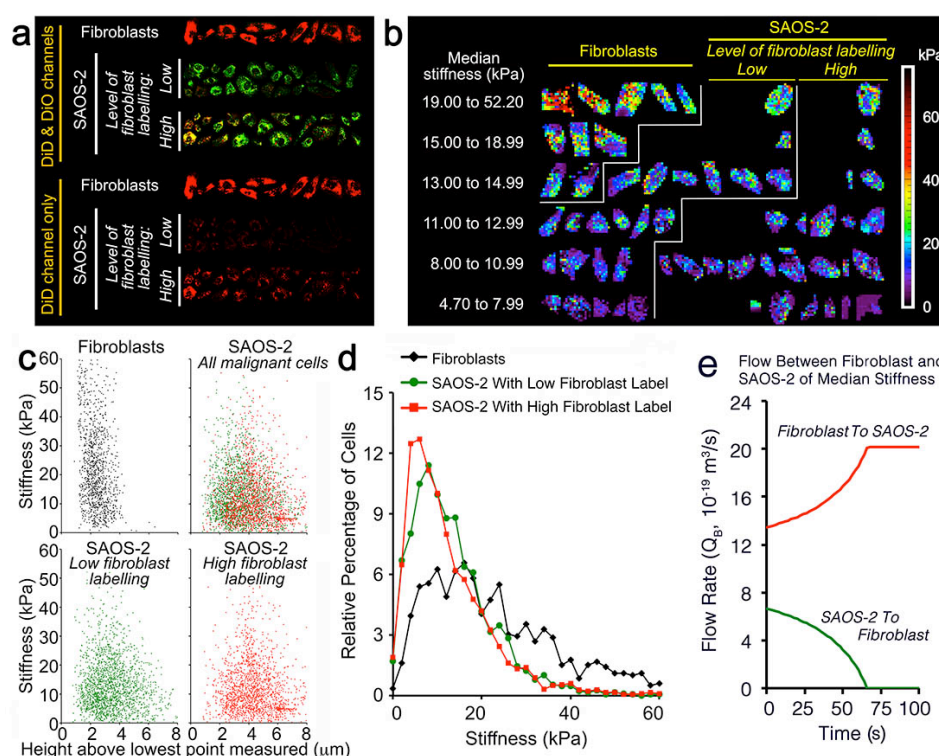


Fig. 4 The relationship between cell stiffness and height in SAOS-2 (pre-labelled with DiO-green) co-cultured for 24 h with fibroblasts (pre-labelled with DiD-red), and mathematical modelling of CPP between cells of median stiffness. (a) DiD (red) levels were quantitated to identify fibroblasts, SAOS-2 with high fibroblast label, and SAOS-2 with low fibroblast label. (b) Although it was not possible to scan the entirety of all cells shown in 'a' by AFM, median values of stiffness scans indicated fibroblasts were stiffer than SAOS-2, and

that SAOS-2 with high fibroblast label were usually less stiff than SAOS-2 with low fibroblast label. (c) This was supported in stiffness fingerprints, demonstrating that fibroblasts (black dots) had greater stiffness and lower cell height compared to SAOS-2 (red and green dots) (Mann Whitney U Test, $p < 0.0001$). Further, stiffness values for SAOS-2 with low fibroblast labeling (green dots) were higher than for SAOS-2 with high fibroblast labelling (red dots), while the reverse was the case with regard to height measurements (Mann Whitney U Test, $p < 0.0004$). (d) Relative percentage distribution plots binned at 2 kPa for stiffness. (e) CPP was modelled between a fibroblast and SAOS-2, each of median cell stiffness, and examining exchange from fibroblast to SAOS-2 (red), as well as from SAOS-2 to fibroblast (green). Results were consistent with the CPP hypothesis.

Label transfer varied in extent amongst SAOS-2, with some SAOS-2 having very high and others negligible fibroblast labeling (Fig. 4a). As predicted, SAOS-2 with high fibroblast labeling had lower stiffness compared with SAOS-2 with low fibroblast labeling (Mann Whitney U Test, $p < 0.0001$).

0.0004) (Fig. 4b,c,d). In addition, higher uptake of fluorescence by CPP correlated with greater cell height (Mann Whitney U Test, $p < 0.0004$).

Fig 4e shows CPP flow rates for transfer from a fibroblast to a SAOS-2, as well as from a SAOS-2 to a fibroblast, assigning median cell stiffness for fibroblasts (18,765 Pa) and SAOS-2 (11,181 Pa), and biologically reasonable assumptions for: cell-projection retraction rate (1×10^{-6} m/s), viscosity (2.5×10^{-3} Pa.s), length at time zero (100 μ m), and radius (0.8 μ m) of the cell-projection. Significant flow was predicted by the mathematical model in these conditions.

Satisfying a further prediction for the CPP model, was that similar to observations in SAOS-2, uptake of fluorescence from SAOS-2 by fibroblasts was negatively correlated with fibroblast cell stiffness, while there was also a positive correlation with cell height (Mann Whitney U Test, $p < 0.0001$) (Fig. 5). Experimental results thus satisfied all predictions from the mathematical model.

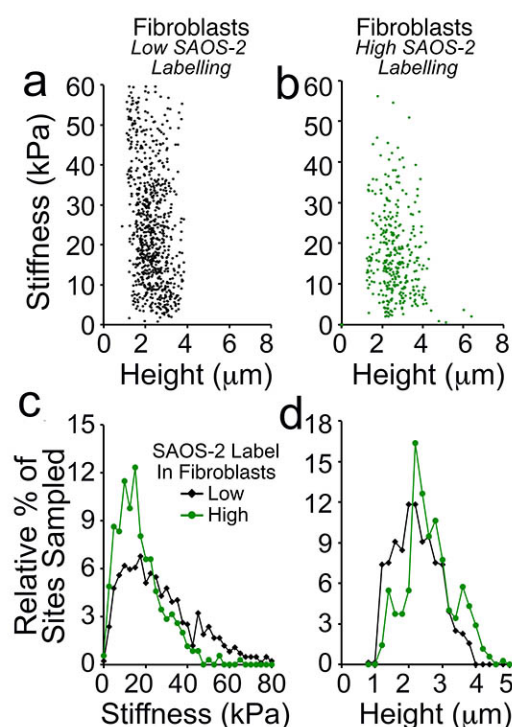


Fig. 5 Stiffness fingerprints and proportional distribution plots comparing stiffness and height AFM measurements for fibroblasts in co-culture with DiO pre-labelled SAOS-2, dependent on whether fibroblasts had high or low levels of SAOS-2 labelling. (a,b) Stiffness fingerprints revealed that fibroblasts with low SAOS-2 labelling had generally higher stiffness and lower cell height measurements (a), compared with fibroblasts with high SAOS-2 labelling (b) (Mann Whitney U Test, $p < 0.0001$). (c,d) Proportional distribution plots binned at 2.5 kPa for stiffness and 0.2 μ m for height measurements, further confirmed the visual impressions from stiffness fingerprints.

3.4 Results of numerical MATLAB simulations agreed with experimental observations and satisfied predictions from the mathematical model

3.4.1 Estimation of stiffness correction factor Z

From equation (30), t_c becomes negative when $L_0/U < |(2Z(F_A - F_B)/(Ca\rho U^2))|$ to generate meaningless negative values for time. To overcome this difficulty, t_c was assigned a value of zero on such occasions during simulations, but since Q_B is maximal at CaU when $t_c=0$ (equations (39, 40, 41), Fig. 3d), this reduces sensitivity of the system to the effect of $(S_A - S_B)$ in varying transfer. Similarly, if Z is chosen such that $|(2Z(F_A - F_B)/(Ca\rho U^2))|$ approaches L_0/U , Q_B approaches $CaU/2$, which although conservative for estimation of total transfer to Receptor Cells B, also fails to fully test the effect of $(S_A - S_B)$.

Preliminary simulations revealed that letting $Z = 1/(\text{median stiffness of all cells A and B considered together})$; (6.9726×10^{-5} in simulations described below); generated values for t_c that were usually positive, and also provided fair testing of the effect of $(S_A - S_B)$ by often positioning t_c in the mid-range between 0 and L_0/U .

3.4.3 Numerical simulations approximated experimental observations

Figs 6a,b shows results of simulations yielding fluorescence transfers closely approximating experimental CPP transfer fluorescence data for both SAOS-2 and fibroblasts, and this concordance was seen making biologically reasonable assumptions for relevant variables. Histograms of input variables, pressures achieved, and both volume and fluorescence transfers are provided in Supplementary Figs. S2 and S3. Median fluorescence levels of donor and receptor cells are shown in Table 1, and demonstrate similarity between experimental and simulated results. Relative fluorescence transfer from fibroblasts to SAOS-2 was greater compared with that from SAOS to fibroblasts in both simulations and by experiment (Table 1).

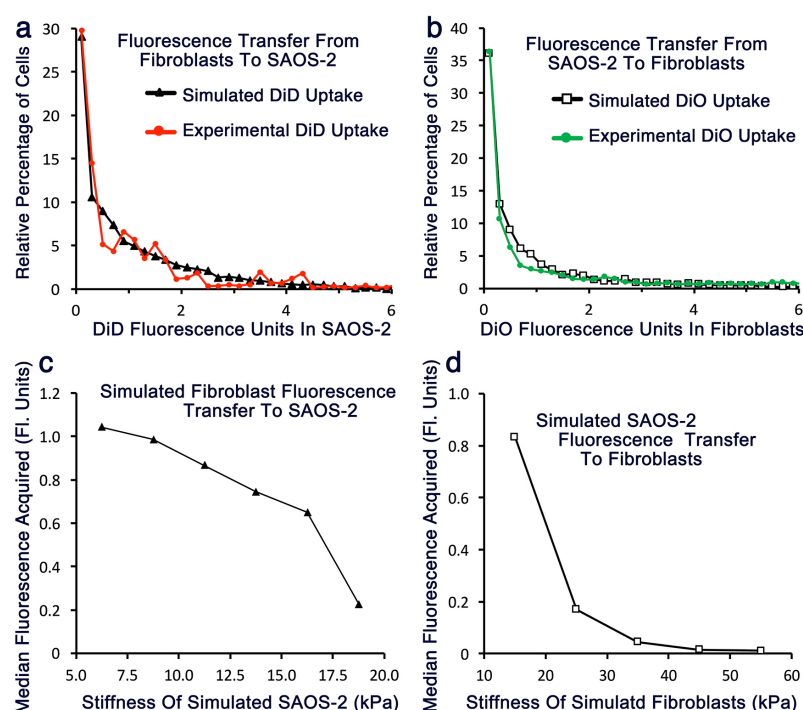


Fig. 6 Graphs comparing exchange of fluorescence between SAOS-2 and fibroblasts observed by experiment (Figs. 4 and 5), with that calculated by numerical simulations for 5000 recipient SAOS-2 or fibroblasts (a,b), and the relationship between recipient cell stiffness and fluorescence uptake (c,d). (a,b) There was good concordance between experimental observations and results of numerical simulations, applying simulation conditions where: the number of donor fibroblasts any given recipient SAOS-2 could interact with ranged from 1 to 3 (1 to 3 for fibroblast recipients); the number of exchange events between individual donor fibroblasts and recipient SAOS-2 cells ranged from 0 to 2, (3 to 8 for recipient fibroblasts); the rate of cell-projection retraction ranged from 0.5 to 1.4 $\mu\text{m/s}$ for donor

fibroblasts, (1 to 5 $\mu\text{m/s}$ for donor SAOS-2); the proportion of maximal possible time for individual transfer events applied ranged from 0 to 0.9 for fibroblast cell-projection retraction (0.6 to 0.9 for SAOS-2 cell-projection retraction); the length of donor cell-projections from donor fibroblasts ranged from 5 to 120 μm , (40 to 90 μm from donor SAOS-2); the radius of fibroblast donor cell-projections was from 0.55 to 1.75 μm , (0.7 to 2.5 μm for donor SAOS-2); and the viscosity of cytoplasm ranged from 1.5 to 4.0 mPa.s for both donor fibroblasts and SAOS-2. (c,d) There was an inverse relationship between SAOS-2 stiffness and median fluorescence acquired by CPP (c), with a similar result for fibroblasts receiving SAOS-2 fluorescence (d) ($p < 0.0001$, Mann Whitney U Test).

Table 1. Median fluorescence levels from experimental observations and simulations

	Median Fluorescence per Cell (Fluorescence Units)			Receptor Fluorescence / Donor Fluorescence	
	Donor Cells	Experimental Receptor Cells	Simulated Receptor Cells	Experimental	Simulated
Red (DiD) Fluorescence	16.904	0.641	0.630	0.038	0.037
Green (DiO) Fluorescence	31.849	0.504	0.414	0.016	0.013

Overall fluorescence levels for simulated receptor cells was comparable to that seen in experimental results. When expressed as ratios relative to donor cell fluorescence, fibroblasts which were the receptors for green DiO fluorescence, had lower uptake relative to red DiD fluorescence by SAOS-2 receptor cells. Proportionate uptake was similar between simulation results and experimental data, with fluorescence uptake of SAOS-2 being 2.40 fold that of fibroblasts (0.038/0.016) by experiment, and 2.81 fold that of fibroblasts by simulation (0.037/0.013).

Consistent with experimental data (Fig. 4), there was an inverse relationship between stiffness and transfer from both fibroblasts to SAOS-2, and also from SAOS-2 to fibroblasts (Fig. 6c,d). Results of simulations thus satisfied all predictions from the mathematical model.

Pressures required for these transfers were generally modest: 1.15×10^{-8} Pa to 212 Pa, with a median value of 0.668 Pa for transfer from fibroblasts to SAOS-2; and 8.98×10^{-11} Pa to 37.3 Pa, with a median value of 0.144 Pa for transfer from SAOS-2 to fibroblasts. Only 2.91% of calculated pressure values were over 10 Pa for transfer from fibroblasts to SAOS-2, while only 0.40% of

calculated pressures were over 10 Pa for transfer from SAOS-2 to fibroblasts. The predominantly low pressures calculated to account for fluorescence transfer, support plausibility for CPP.

3.5 Simulations predicted large proportional volume transfers between cells

Data on volume exchange were expressed as percentages relative to the average volume of a single Receptor Cell B SAOS-2 or fibroblast. Table 2 shows results for volume transfers in the same simulations illustrated in Fig. 6. Most simulated cells in recipient populations accepted appreciable volumes of donor cell cytoplasm. Simulated proportional volume transfers to fibroblasts were generally lower than those calculated for SAOS-2 (Table 2).

4 Discussion

All predictions that follow from the CPP hypothesis and mathematical model were satisfied by either experiment or simulations. Taken together, these differing data support CPP as a previously unrecognized mechanism for inter-cellular cytoplasmic exchange, and we suggest the current work forms a reasonable theoretical framework for further investigation. Further, the hydrodynamic mechanism we propose for CPP through equilibration of local pressure differentials by cytoplasmic flow is in some ways similar to that described in formation of lamellipodia³³, blebbing^{34,35}, and the formation of lobopodia³⁶.

We favored the CPP hypothesis over of an alternative interpretation of CLSM images, in which transfer could have been via ‘cell-projection budding and phagocytosis’. Notably, CPP modelling predicted an inverse relationship between receptor cell stiffness and transfer that was confirmed by experiment, while no such relationship would be expected were the cytoplasmic transfers seen due to a budding and phagocytosis mechanism.

TNT differ fundamentally from the cell-projections observed to be responsible for CPP in the current study. Whereas cell-projections mediating CPP presented as transient, short, and branching structures, mechanically supported by the culture surface or cells; TNT often persist hours, extend long distances, are non-branching, and are suspended free above the culture surface^{11,12,16,19-23}. While delivery of surface signals and directed migration are known roles for specialized filopodia³⁷, cytoplasmic transfer via cell-projections in the size range of filopodia seems a novel function. Some precedent is, however, established by filopodial transfer of melanosomes, but precise details of melanosome transfer remain uncertain and phagocytosis of shed melanosomes may occur³⁸⁻⁴⁰. It would be interesting to determine if CPP contributes to melanosome transfer. Similarly, the mechanism whereby mitochondria are transferred between mammalian cells remains unclear^{5-10,18}, and we speculate that CPP contributes to this important process.

We have separately demonstrated TNT in MC²⁰⁻²², and also showed increased TNT on exposure to exosomes²⁵, but consistent with our initial report¹, neither TNT or exosomes could account for the current observations. Uptake of fibroblast label by MC was not only inconsistent with exosome or TNT transfer, but was also not accounted for on basis of non-specific DiD (red) label diffusion, or phagocytosis of fibroblast cell fragments. In addition, the deep grooving of MC by fibroblast cell-projections was indicative of a significant difference in cell stiffness, further confirmed by AFM and correlated with the extent of cytoplasmic exchange. The asymmetry in exchange seen experimentally between fibroblasts and SAOS-2 was consistent with our earlier published observations¹.

We earlier noted phenotypic changes associated with inter-cellular cytoplasmic and membrane transfer^{1,14,15}, and suggest CPP plays a role in this. In addition, the appreciable volumes of SAOS-2 cytoplasm transferred to fibroblasts in simulations, suggests a possible role for CPP in development of cancer-associated fibroblasts, which are increasingly recognized as important for cancer development⁴¹.

Numerical modelling permitted estimation of the volumes of cytoplasmic transfer required to account for exchange in co-culture, previously not possible due to diversity in donor cell fluorescence. The appreciable relative volume transfers seen in Table 2 were consistent with the high fluorescence exchange visually apparent in experiments¹ (Figs. 1,2,4).

Although we do believe our approach to mathematical modeling is reasonable, there are some aspects that bear further discussion. Turbulent flow is near impossible in the range of radius

Table 2. The proportionate percentage distribution of recipient SAOS-2 and fibroblasts, according to the volume acquired from the opposing cell type in simulated co-culture generating fluorescence profiles approximating those seen by experiment, expressed as percentages relative to the average volume of the respective recipient cell type.

% Volume Relative to Average Recipient Cell	Simulated SAOS-2 Number	% Relative to All Simulated SAOS-2	% of Simulated SAOS-2 with Transfer over Threshold	Simulated Fibroblast Number	% Relative to All Simulated Fibroblasts	% of Simulated Fibroblasts with Transfer over Threshold
0 to < 1	1301	26.02	100	2062	41.26	100
1 to < 3	925	18.5	73.98	1274	25.46	58.74
3 to < 5	661	13.22	55.48	523	10.46	33.28
5 to < 7	455	9.1	42.26	263	5.26	22.82
7 to < 9	376	7.52	33.16	176	3.54	17.56
9 to < 11	312	6.24	25.64	135	2.58	14.02
11 to < 13	232	4.64	19.4	141	2.82	11.44
13 to < 15	205	4.1	14.76	110	2.26	8.62
15 to < 17	164	3.28	10.66	88	1.76	6.36
17 to < 19	110	2.2	7.38	80	1.6	4.6
19 to < 21	64	1.28	5.18	52	1.08	3
21 to < 23	64	1.28	3.9	26	0.52	1.92
23 to < 25	45	0.9	2.62	21	0.42	1.4
25 to < 27	23	0.46	1.72	19	0.38	0.98
27 to < 29	21	0.42	1.26	16	0.32	0.6
29 to < 31	15	0.3	0.84	4	0.08	0.28
31 to < 33	6	0.12	0.54	0	0	0.2
33 to < 35	11	0.22	0.42	3	0.06	0.2
35 to < 37	3	0.06	0.2	4	0.08	0.14
37 to < 39	1	0.02	0.14	0	0	0.06
39 to < 41	3	0.06	0.12	2	0.04	0.06
41 to < 43	0	0	0.06	0	0	0.02
43 to < 45	2	0.04	0.06	0	0	0.02
45 to < 47	1	0.02	0.02	0	0	0.02
47 to < 49	0	0	0	1	0.02	0.02
Total	5000	100		5000	100	

Simulations predicting fluorescence profiles for recipient cells similar to experimental results (Fig. 6), also predicted transfer of appreciable volumes of cytoplasm to recipient cells. 55.5% of simulated SAOS-2 had over 3%, and 5.2% of SAOS-2 had over 19% volume acquired from simulated fibroblasts. Consistent with occasional experimentally observed SAOS-2 with very high fibroblast DiD labelling, 10 simulated SAOS-2 cell acquired between 35% and 47% of their volume from simulated fibroblasts. Simulated fibroblasts also acquired appreciable cytoplasm from simulated SAOS-2, but this was generally less compared with exchange in the reverse direction.

values used, lending confidence to use of the Hagen-Poiseuille equation in our model. Cytoplasmic viscosity is non-uniform and dependent on scale, with viscosity being very low but varying across micro-volumes of the cell dependent on contents, and increasing to high levels when measured at the whole cell level due to the admixture of organelles and cytoskeletal elements^{31,32,42}. At the scale modeled in the current study, cytoplasm has viscosity ranging upwards from that close to

water, in the ranges approximately from 1 to 4 mPa.s^{31,32}, and this is reflected by the values we used for this variable. The effect of organelles suspended in cytoplasm is, however, more difficult to anticipate. We suggest that although cytoplasm itself at the scale studied may have very low viscosity in the order of 1.5 mPa.s, that by including higher viscosity values in simulations, we have made reasonable accommodation for the effect of suspended organelles.

In preliminary simulations not shown, we assumed a normal distribution between target minima and maxima for variables other than stiffness and fluorescence, and observed 'a central hump' in the resulting simulated fluorescence profiles, inconsistent with experimental fluorescence. Weakening the central tendency by spreading the distribution of variables to a flattened profile, achieved simulation results more in keeping with experimental data, and this suggests a uniform distribution for key variables *in-vivo*. Confirmation of this inference awaits improved structural and temporal resolution of events in living cells. Modest divergence of simulated from experimental results, likely reflects limitations inherent to the model, including possible skewedness and unknown dependencies between variables.

While acknowledging the limitations of our analysis discussed above, we do feel it is reasonable to advance our hypothesis of CPP between mammalian cells. Not only does CPP seem to be a previously unrecognized biological process, but our earlier work suggests CPP results in significant phenotypic change^{1,15}, and this has direct relevance to generation of tumor cell diversity and hence progression of malignancy.

Not addressed in the current work, is the basis for formation of the transient inter-cellular cytoplasmic continuities through which cytoplasm must pass between cells. We have no current data on this point, but speculate that these may form through membrane fusion mechanisms. Although CPP does not appear to involve TNT, it is of note that TNT do evidence capacity of neighboring cells to establish the inter-cellular cytoplasmic continuities necessary for CPP to occur.

It is unlikely that CPP would be confined to interactions between fibroblasts and MC, while we earlier observed uptake of cytoplasm from smooth muscle cells by MC (unpublished results). Cancer only rarely seems to generate truly new biology, but instead appears to pervert established biological mechanisms. For these reasons, we think it highly likely that CPP plays an important role in cell differentiation and phenotypic control in other biological settings including embryogenesis, development, inflammation and wound healing, consistent with reports of inter-cellular exchange by both reported and as yet unresolved mechanisms^{1-16,18-25,38-40}. We believe our current work forms a useful platform from which to explore these further interesting possibilities.

Acknowledgements

We thank the Memorial Sloan Kettering Cancer Center, including via MSKCC P30 CA008748 Cancer Center Support Grant, as well as the Australian Dental Research Fund for their support of this work. We also thank an anonymous donor for their generous contribution. In addition, we thank Dr R Norden of the Graduate School of Biomedical Engineering, The University of NSW, for his advice.

Compliance with ethical standards

The authors declare no competing interests. Experiments were performed with commercially sourced human dermal fibroblasts (Coriell Institute, Cambden, NJ), while malignant cells were either from the American Type Culture Collection (SAOS-2, VA, USA) or the collection of the Westmead Institute of Medical Research (Westmead, NSW, Australia), so that no human ethics approval was required. Experiments were performed in accordance with relevant guidelines and regulations.

References

- 1 David, M. S. *et al.* Membrane and cytoplasmic marker exchange between malignant neoplastic cells and fibroblasts via intermittent contact: increased tumour cell diversity independent of genetic change. *J Pathol* **228**, 495-505, doi:10.1002/path.4063 (2012).
- 2 Sinclair, K. A., Yerkovich, S. T., Hopkins, P. M. & Chambers, D. C. Characterization of intercellular communication and mitochondrial donation by mesenchymal stromal cells derived from the human lung. *Stem Cell Res Ther* **7**, 91, doi:10.1186/s13287-016-0354-8 (2016).
- 3 Lehmann, T. P. *et al.* Coculture of human nucleus pulposus cells with multipotent mesenchymal stromal cells from human bone marrow reveals formation of tunnelling nanotubes. *Mol Med Rep* **9**, 574-582, doi:10.3892/mmr.2013.1821 (2014).
- 4 Lehmann, T. P. *et al.* Quantification of the asymmetric migration of the lipophilic dyes, DiO and DiD, in homotypic co-cultures of chondrosarcoma SW-1353 cells. *Mol Med Rep* **14**, 4529-4536, doi:10.3892/mmr.2016.5793 (2016).
- 5 Pasquier, J. *et al.* Preferential transfer of mitochondria from endothelial to cancer cells through tunneling nanotubes modulates chemoresistance. *Journal of translational medicine* **11**, 94, doi:10.1186/1479-5876-11-94 (2013).
- 6 Islam, M. N. *et al.* Mitochondrial transfer from bone-marrow-derived stromal cells to pulmonary alveoli protects against acute lung injury. *Nat Med* **18**, 759-765, doi:10.1038/nm.2736 (2012).
- 7 Liu, K. *et al.* Mesenchymal stem cells rescue injured endothelial cells in an in vitro ischemia-reperfusion model via tunneling nanotube like structure-mediated mitochondrial transfer. *Microvasc Res* **92**, 10-18, doi:10.1016/j.mvr.2014.01.008 (2014).
- 8 Spees, J. L., Olson, S. D., Whitney, M. J. & Prockop, D. J. Mitochondrial transfer between cells can rescue aerobic respiration. *Proc Natl Acad Sci U S A* **103**, 1283-1288, doi:10.1073/pnas.0510511103 (2006).
- 9 Vallabhaneni, K. C., Haller, H. & Dumler, I. Vascular smooth muscle cells initiate proliferation of mesenchymal stem cells by mitochondrial transfer via tunneling nanotubes. *Stem Cells Dev* **21**, 3104-3113, doi:10.1089/scd.2011.0691 (2012).
- 10 Koyanagi, M., Brandes, R. P., Haendeler, J., Zeiher, A. M. & Dimmeler, S. Cell-to-cell connection of endothelial progenitor cells with cardiac myocytes by nanotubes: a novel mechanism for cell fate changes? *Circulation research* **96**, 1039-1041, doi:10.1161/01.RES.0000168650.23479.0c [pii] 10.1161/01.RES.0000168650.23479.0c (2005).
- 11 Davis, D. M. & Sowinski, S. Membrane nanotubes: dynamic long-distance connections between animal cells. *Nat Rev Mol Cell Biol* **9**, 431-436, doi:10.1038/nrm2399 (2008).
- 12 Gerdes, H. H., Rustom, A. & Wang, X. Tunneling nanotubes, an emerging intercellular communication route in development. *Mech Dev* **130**, 381-387, doi:10.1016/j.mod.2012.11.006 (2013).
- 13 Onfelt, B. *et al.* Structurally distinct membrane nanotubes between human macrophages support long-distance vesicular traffic or surfing of bacteria. *J Immunol* **177**, 8476-8483 (2006).
- 14 David, M. S. *et al.* SAOS-2 osteosarcoma cells bind fibroblasts via ICAM-1 and this is increased by tumour necrosis factor-alpha. *PLoS One* **9**, e101202, doi:10.1371/journal.pone.0101202 (2014).
- 15 David, M. S., Kelly, E. & Zoellner, H. Opposite cytokine synthesis by fibroblasts in contact co-culture with osteosarcoma cells compared with transwell co-cultures. *Cytokine* **62**, 48-51, doi:10.1016/j.cyto.2013.02.028 (2013).
- 16 Bloemendal, S. & Kuck, U. Cell-to-cell communication in plants, animals, and fungi: a comparative review. *Die Naturwissenschaften* **100**, 3-19, doi:10.1007/s00114-012-0988-z (2013).
- 17 Caneparo, L., Pantazis, P., Dempsey, W. & Fraser, S. E. Intercellular bridges in vertebrate gastrulation. *PLoS One* **6**, e20230, doi:10.1371/journal.pone.0020230 (2011).
- 18 Herst, P. M., Dawson, R. H. & Berridge, M. V. Intercellular communication in tumour biology: A role for mitochondrial transfer. *Frontiers in oncology* **8**, 344-353, doi:10.3389/fonc.2018.00344 (2018).
- 19 Ahmed, K. A. & Xiang, J. Mechanisms of cellular communication through intercellular protein transfer. *J Cell Mol Med* **15**, 1458-1473, doi:10.1111/j.1582-4934.2010.01008.x [pii] 10.1111/j.1582-4934.2010.01008.x (2011).
- 20 Ady, J. W. *et al.* Intercellular communication in malignant pleural mesothelioma: properties of tunneling nanotubes. *Frontiers in physiology* **5**, 400, doi:10.3389/fphys.2014.00400 (2014).
- 21 Lou, E. *et al.* Tunneling Nanotubes: A new paradigm for studying intercellular communication and therapeutics in cancer. *Communicative & integrative biology* **5**, 399-403, doi:10.4161/cib.20569 (2012).

- 22 Lou, E. *et al.* Tunneling nanotubes provide a unique conduit for intercellular transfer of cellular contents in human malignant pleural mesothelioma. *PLoS One* **7**, e33093, doi:10.1371/journal.pone.0033093 (2012).
- 23 Ariazi, J. *et al.* Tunneling Nanotubes and Gap Junctions-Their Role in Long-Range Intercellular Communication during Development, Health, and Disease Conditions. *Front Mol Neurosci* **10**, 333, doi:10.3389/fnmol.2017.00333 (2017).
- 24 Delage, E. *et al.* Differential identity of Filopodia and Tunneling Nanotubes revealed by the opposite functions of actin regulatory complexes. *Scientific reports* **6**, 39632, doi:10.1038/srep39632 (2016).
- 25 Thayanithy, V. *et al.* Tumor exosomes induce tunneling nanotubes in lipid raft-enriched regions of human mesothelioma cells. *Exp Cell Res* **323**, 178-188, doi:10.1016/j.yexcr.2014.01.014 (2014).
- 26 Zoellner, H., Paknejad, N., Manova, K. & Moore, M. A. A novel cell-stiffness-fingerprinting analysis by scanning atomic force microscopy: comparison of fibroblasts and diverse cancer cell lines. *Histochem Cell Biol* **144**, 533-542, doi:10.1007/s00418-015-1363-x (2015).
- 27 Darby, R. & Chhabra, R. P. *Chemical engineering fluid mechanics*. 3 edn, (CRC Press, 2016).
- 28 Law, J. & Rennie, R. in *A dictionary of physics* (eds J. Law & R. Rennie) (Oxford University Press, Oxford, 2009).
- 29 Feneberg, W., Westphal, M. & Sackmann, E. Dictyostelium cells' cytoplasm as an active viscoplastic body. *Eur Biophys J* **30**, 284-294 (2001).
- 30 Barthel, E. Adhesive elastic contacts - JKR and more. *Journal of Physics D: Applied Physics* **41**, 163001-163041, doi:10.1088/0022-3727/41/16/163001 (2008).
- 31 Fushimi, K. & Verkman, A. S. Low viscosity in the aqueous domain of cell cytoplasm measured by picosecond polarization microfluorimetry. *J Cell Biol* **112**, 719-725 (1991).
- 32 Kalwarczyk, T. *et al.* Comparative analysis of viscosity of complex liquids and cytoplasm of mammalian cells at the nanoscale. *Nano letters* **11**, 2157-2163, doi:10.1021/nl2008218 (2011).
- 33 Manoussaki, D., Shin, W. D., Waterman, C. M. & Chadwick, R. S. Cytosolic pressure provides a propulsive force comparable to actin polymerization during lamellipod protrusion. *Scientific reports* **5**, 12314, doi:10.1038/srep12314 (2015).
- 34 Charras, G. T., Yarrow, J. C., Horton, M. A., Mahadevan, L. & Mitchison, T. J. Non-equilibration of hydrostatic pressure in blebbing cells. *Nature* **435**, 365-369, doi:10.1038/nature03550 (2005).
- 35 Strychalski, W. & Guy, R. D. Intracellular Pressure Dynamics in Blebbing Cells. *Biophys J* **110**, 1168-1179, doi:10.1016/j.bpj.2016.01.012 (2016).
- 36 Petrie, R. J., Gavara, N., Chadwick, R. S. & Yamada, K. M. Nonpolarized signaling reveals two distinct modes of 3D cell migration. *J Cell Biol* **197**, 439-455, doi:10.1083/jcb.201201124 (2012).
- 37 Fairchild, C. L. & Barna, M. Specialized filopodia: at the 'tip' of morphogen transport and vertebrate tissue patterning. *Curr Opin Genet Dev* **27**, 67-73, doi:10.1016/j.gde.2014.03.013 (2014).
- 38 Scott, G., Leopardi, S., Printup, S. & Madden, B. C. Filopodia are conduits for melanosome transfer to keratinocytes. *J Cell Sci* **115**, 1441-1451 (2002).
- 39 Singh, S. K. *et al.* Melanin transfer in human skin cells is mediated by filopodia--a model for homotypic and heterotypic lysosome-related organelle transfer. *FASEB J* **24**, 3756-3769, doi:10.1096/fj.10-159046 (2010).
- 40 Ma, H. J. *et al.* alpha-Melanocyte stimulating hormone (MSH) and prostaglandin E2 (PGE2) drive melanosome transfer by promoting filopodia delivery and shedding spheroid granules: Evidences from atomic force microscopy observation. *J Dermatol Sci* **76**, 222-230, doi:10.1016/j.jdermsci.2014.09.005 (2014).
- 41 LeBleu, V. S. & Kalluri, R. A peek into cancer-associated fibroblasts: origins, functions and translational impact. *Dis Model Mech* **11**, doi:10.1242/dmm.029447 (2018).
- 42 Plaza, G. R. *et al.* Simple measurement of the apparent viscosity of a cell from only one picture: Application to cardiac stem cells. *Phys Rev E Stat Nonlin Soft Matter Phys* **90**, 052715, doi:10.1103/PhysRevE.90.052715 (2014).